



Fe₃O₄@MIL-100(Fe) modified ZnS nanoparticles with enhanced sonocatalytic degradation of tetracycline antibiotic in water

Kai Zhang^a, Jingjing Zhang^b, Xue He^b, Yue Zhao^b, Amir Zada^{c,*}, Anzhong Peng^{b,*}, Kezhen Qi^{b,*}

^a College of Biochemistry and Environmental Engineering, Baoding University, Baoding 071000, China

^b College of Pharmacy, Dali University, Dali 671000, Yunnan, China

^c Department of Chemistry, Abdul Wali Khan University, Mardan, Khyber Pakhtunkhwa, 23200, Pakistan

ARTICLE INFO

Keywords:

Fe₃O₄@MIL-100(Fe)

ZnS

Hybridization

Acoustic catalytic removal

Tetracycline

ABSTRACT

Sonocatalysis has attracted excellent research attention to eradicate hazardous pollutants from the environment effectively. This work synthesised an organic/inorganic hybrid composite catalyst by coupling Fe₃O₄@MIL-100(Fe) (FM) with ZnS nanoparticles using the solvothermal evaporation method. Remarkably, the composite material delivered significantly enhanced sonocatalytic efficiency for removing tetracycline (TC) antibiotics in the presence of H₂O₂ compared to bare ZnS nanoparticles. By adjusting different parameters such as TC concentration, catalyst dosage and H₂O₂ amount, the optimized composite (20 %Fe₃O₄@MIL-100(Fe)/ZnS) removed 78.25% antibiotic in 20 min at the cost of 1 mL of H₂O₂. These much superior activities are attributed to the efficient interface contact, effective charge transfer, accelerated transport capabilities and strong redox potential for the superior acoustic catalytic performance of FM/ZnS composite systems. Based on various characterization, free radical capture experiments and energy band structures, we proposed a mechanism for the sonocatalytic degradation of tetracycline based on S-scheme heterojunctions and Fenton like reactions. This work will provide an important reference for developing ZnS-based nanomaterials to study sonodegradation of pollutants.

1. Introduction

Environmental pollution, including water, air, and soil, has gathered huge concern amongst the scientific community [1]. Many organic dyes, domestic wastewater, antibiotics, and other substances have caused incurable animal and plant diseases [2–4]. Antibiotics are largely used to inhibit microorganisms' growth, preventing many fatal diseases in humans and animals [5]. However, a considerable amount of the precursor materials is directly discharged to the nearby water bodies during the synthesis of antibiotics. Further, the animals absorb and assimilate a very small portion of these lifesaving antibiotics during their antibiotic treatment.

In contrast, a huge portion is excreted as metabolites during faeces and urination. Ultimately, these antibiotics find their way into the soil and water environment causing their slow accumulation to pollute the environment. In addition, antibiotics induce the production of resistant microorganisms and resistant genes, leading to drug resistance in organisms through transmission and diffusion [6]. Tetracycline (TC) is the

most widely used low-cost broad-spectrum antibiotic with high antibacterial activity. It has multiple effects, such as growth promotion, tumour treatment and promoting bone absorption [7]. It has been widely detected in surface, groundwater, and drinking water. Considering its hazardous effects, developing efficient and simple antibiotic removal technologies is crucial [8].

Traditional TC removal technologies, including biodegradation, physical adsorption, electrochemical degradation, and advanced oxidation, are largely characterized by their complex nature, high economic costs and the required length of time as their main disadvantages [9–11]. Therefore, these techniques received little appreciation in the scientific community. Recently, the sono-catalytic technique has shown unique advantages in removing hazardous pollutants from an aqueous environment. The sonocatalytic oxidation process degrades organic pollutants in a very short time. Under the cavitation effect of ultrasound in the presence of semiconductor materials, the generated water vapour in the cavitation bubble undergoes pyrolysis at high temperature and pressure to form free radicals such as $\cdot\text{OH}$ and $\cdot\text{O}_2^-$. Under shock waves

* Corresponding authors.

E-mail addresses: amistry009@yahoo.com (A. Zada), penganzhong@dali.edu.cn (A. Peng), qkzh2003@aliyun.com (K. Qi).

<https://doi.org/10.1016/j.ultsonch.2023.106409>

Received 30 March 2023; Received in revised form 13 April 2023; Accepted 16 April 2023

Available online 18 April 2023

1350-4177/© 2023 The Authors. Published by Elsevier B.V. This is an open access article under the CC BY-NC-ND license (<http://creativecommons.org/licenses/by-nc-nd/4.0/>).

and jets generated during the collapse of the cavitation bubble, extremely strong oxidizing agents are produced, which participate in the acoustic catalytic oxidation degradation of pollutants to convert them into harmless CO_2 , H_2O , inorganic acids, etc. [12]. Many composite materials such as $\text{BiOBr}/\text{BiFeO}_3$, $\text{BiOBr}/\text{FeWO}_4$ and MoS_2/CNTs have shown excellent activities in the sonocatalytic removal of antibiotics [13–15]. Amongst various materials, ZnS is an important direct broad-band gap semiconductor with strong redox potentials of the conduction and valence bands. It has shown excellent services in the sono/photo-catalytic degradation of pollutants from water [16]. Mandal et al. studied the sonocatalytic degradation of RhB using spherical ZnS as a semiconductor, and the measured degradation efficiency was 64% [17]. However, after forming a heterojunction with g- C_3N_4 , the degradation efficiency improved by up to 92%, attributed to the improved charge separation. However, the catalytic performance of ZnS is still limited, attributed to its low energy absorption and high charge recombination. Many researchers used supported cocatalysts as an effective strategy to improve the catalytic activity of ZnS nanoparticles. In this regard, $\text{Fe}_3\text{O}_4@\text{MIL-100}(\text{Fe})$ is an excellent candidate to be coupled with ZnS, considering the synergetic effect of sonocatalysis and Fenton-like reactions [18]. In sonocatalysis with ZnS, constructing organic–inorganic hybrid nano-systems is conducive to achieving efficient charge transfer and energy conversion. The interaction between interfaces further promotes the redox reaction over the catalyst surface [19].

This work used the solvent evaporation method to synthesize $\text{Fe}_3\text{O}_4@\text{MIL-100}(\text{Fe})/\text{ZnS}$ nanocomposites for the sonocatalytic degradation of tetracycline antibiotics. Different mass ratios of FM were loaded on the surface of ZnS nanoparticles, and their sonocatalytic activities were monitored. The catalyst's morphology, photoelectric property and energy band structure were characterized and analyzed by XRD, FTIR, XPS, TEM, BET and electrochemical characterization. It has been found that 20FM/ZnS has excellent optical absorption performance, efficient charge transfer rate and increased specific surface area. Combining energy band structure and free radical capture experiments, we proposed a possible Fenton like synergistic sonocatalytic degradation mechanism. At the same time, the S-scheme heterojunction between FM and ZnS provides a shorter charge transfer path and retains the strong redox potential of ZnS. The Fenton-like reaction of a small amount of Fe^{2+} and Fe^{3+} accelerates the sonocatalytic degradation process of TC over ZnS.

2. Experimental section

2.1. Materials

Zinc nitrate ($\text{Zn}(\text{NO}_3)_2 \cdot 6\text{H}_2\text{O}$ AR), iron nitrate nonahydrate ($\text{Fe}(\text{NO}_3)_3 \cdot 9\text{H}_2\text{O}$ AR), sodium sulfate (Na_2SO_4 AR), barium sulfate (BaSO_4 AR), FeCl_3 , sodium citrate, and sodium acetate were purchased from Sinopharm Chemical Reagents Co., Ltd. Trimesic acid (H_3BTC) and tetracycline ($\text{C}_{22}\text{H}_{24}\text{N}_2\text{O}_8$ AR) were purchased from McLean Reagent Co., Ltd., sodium sulfide ($\text{Na}_2\text{S} \cdot 9\text{H}_2\text{O}$ AR) was purchased from Nanjing Chemical Reagent Co., Ltd., and anhydrous ethanol, ethylene glycol and ethylene diamine were purchased from Xilong Scientific Reagent Co., Ltd.

2.2. Synthesis of ZnS

5 mmol $\text{Zn}(\text{NO}_3)_2$ and 10 mmol Na_2S solutions were prepared with 80 mL of a 2:1:1 mixture of water, ethanol and ethylenediamine. After magnetic stirring at room temperature for 30 min, both solutions were mixed and transferred to a 100 mL autoclave. The autoclave was heated at 180 °C for 12 h. The white precipitate formed was cooled naturally to room temperature, washed twice with water and ethanol, and dried at 60 °C in an oven. The obtained milky white ZnS nanoparticles were stored for further experimental work.

2.3. Synthesis of $\text{Fe}_3\text{O}_4@\text{MIL-100}(\text{Fe})$

According to the reported literature [20], Fe_3O_4 nanoparticles were synthesized through coprecipitation by dissolving certain amounts of FeCl_3 , sodium citrate and sodium acetate as raw materials in 80 mL ethylene glycol. The raw materials were allowed to react for 10 h in an oven at 200 °C to obtain Fe_3O_4 nanoparticles. $\text{Fe}_3\text{O}_4@\text{MIL-100}(\text{Fe})$ was synthesized by mixing a certain amount of Fe_3O_4 and $\text{Fe}(\text{NO}_3)_3 \cdot 9\text{H}_2\text{O}$ to 30 mL deionized water under stirring at room temperature for 1 h. About 7 g H_3BTC were added under ultrasonic dissolution and the resultant mixture was allowed to react at 95 °C for 10 h to obtained orange colored precipitate. The precipitate was washed with hot water and vacuum dried to get the final product.

2.4. Synthesis of $\text{Fe}_3\text{O}_4@\text{MIL-100}(\text{Fe})/\text{ZnS}$

A certain amount of ZnS nanoparticles and $\text{Fe}_3\text{O}_4@\text{MIL-100}(\text{Fe})$ was added to 40 mL water/ethanol mixed solvent system under stirring at 80 °C for 1 h. The mixture was cooled and filtered to collect the final product. Following the same procedure, $\text{Fe}_3\text{O}_4@\text{MIL-100}(\text{Fe})/\text{ZnS}$ composite catalysts with different mass ratios (10, 15, 18, 20 and 22 wt %) of $\text{Fe}_3\text{O}_4@\text{MIL-100}(\text{Fe})$ were prepared and abbreviated as xFM/ZnS where x shows the percent mass of $\text{Fe}_3\text{O}_4@\text{MIL-100}(\text{Fe})$ in the composites.

2.5. Characterization

Bruker X-ray powder diffractometer (XRD) with Cu-K α as the radiation source ($\lambda = 1.5406 \text{ \AA}$) was used at the scanning range of 5–90° to measure the crystal phase information of the catalyst. Using spectra of pure KBr as the background, the chemical structure of the catalyst was measured by taking Fourier transform infrared (FTIR) spectra with a scan range of 400–4000 cm^{-1} and a resolution of 4 cm^{-1} . The surface elemental composition and the existing state of the constituent elements were analyzed by X-ray photoelectron spectroscopy (XPS). The morphology and elemental composition of the catalysts were analyzed using transmission electron microscopy, high-resolution transmission electron microscopy and EDS. Using BaSO_4 as a reference, the optical absorption performance of the material was characterized by TU-1901 ultraviolet–visible diffuse reflectance spectroscopy (UV–vis DRS) in the scanning range of 200–800 nm. The catalyst's photoluminescence spectrum (PL) was measured at 380 nm excitation wavelength using an RF-5301PC fluorescence spectrometer. Brunauer–Emmett–Teller (BET) surface areas were determined in a Beckman Coulter BSD-660 instrument. Before the experiments, samples were degassed at 200 °C for 2 h until a 10–7 Torr pressure was reached.

2.6. Sonocatalytic degradation of tetracycline

The sonocatalytic degradation performance of the synthesized catalysts was investigated by taking tetracycline antibiotics as a pollutant in an aqueous solution. The entire experiment was conducted with an ultrasonic instrument (SB25-12D). About 30 mg of catalyst was added to 50 mL (30 mg/L) of tetracycline solution. The mixture was placed in the dark and stirred for 30 min to achieve an adsorption–desorption equilibrium between the catalyst surface and tetracycline. Subsequently, the mixture was transferred to an ultrasound instrument, and 1 mL H_2O_2 was added and exposed to ultrasound for 20 min. About 5 mL sample was taken every 4 min, and the supernatant was centrifuged (9000 rpm, 6 min). The absorbance value was measured at the maximum absorption peak of 357 nm using a TU-1901 ultraviolet–visible spectrophotometer. The degradation of the tetracycline was calculated using $A_0 - A_t / A_0 \times 100$ where A_0 and A_t are the absorbance values of TC after ultrasonic treatment for '0' min and 't' min respectively.

2.7. Investigation of the influencing factors

This work also investigated the factors affecting the optimised catalyst's ultrasonic catalytic activity. Following the same procedure as described for the sonocatalytic degradation of tetracycline in section 2.6, the effects of change in the amount of catalyst (15–35 mg), the concentration of tetracycline (20–40 mg/L), the amount of H_2O_2 (0–2 mL), and pH on the activity of acoustic catalytic removal of TC were investigated using the optimized 20FM/ZnS catalyst.

2.8. Active species capture experiment

The chief active species responsible for the degradation of the TC antibiotic were investigated using the optimized 20FM/ZnS catalyst. Following the same procedure as described for the sonocatalytic degradation of tetracycline in section 2.6, 1 mL each of 0.01 mol/L p-benzoquinone solution (BQ), n-butanol solution (n-BA), 0.01 mol/L disodium ethylenediaminetetraacetic acid solution (EDTA-2Na), and 0.01 mol/L potassium persulfate (KPS) were added to the reaction mixture as the trapping agents to deceive superoxide radicals (O_2^-), hydroxyl radicals (OH^\cdot), holes (h^+) and electrons (e^-) respectively [21]. The absorbance values of the TC solution before and after ultrasonic irradiation were measured to identify the main active species in the degradation process.

2.9. Photochemical test

The photoelectric properties like flat band potential, transient photocurrent (I-t) and impedance spectroscopy (EIS) tests of ZnS, FM and 20FM/ZnS catalysts were characterized to investigate charge transfer in the prepared composites. Using an electrochemical workstation (CHI660D) device, tests were conducted in a three-electrode system consisting of platinum wire as a counter electrode, saturated calomel electrode as a reference electrode, and indium tin oxide (ITO) conductive glass coated with sample (10 mm × 20 mm) as the working electrode. For the measurement of the flat band potential and photocurrent tests, 0.1 M Na_2SO_4 solution has used as an electrolyte, while for AC impedance spectroscopy, the electrolyte solution was a 0.1 M KCl solution prepared by dissolving an exact amount of $\text{K}_3[\text{Fe}(\text{CN})_6]$ and $\text{K}_4[\text{Fe}(\text{CN})_6]$ in 1:1 ratio.

3. Results and discussion

3.1. Xrd

Fig. 1 shows the XRD diffraction patterns of ZnS, FM and FM/ZnS catalysts. The results show that the characteristic diffraction peaks of ZnS are located at 26.8, 28.5, 30.5, 39.6, 47.5, 51.7 and 56.4° corresponding respectively to the (100), (002), (101), (102), (110), (103) and (112) crystal planes of wurtzite ZnS (JCPDS No. 36-1450) [22]. The XRD diffraction peaks of FM are located at 10.8, 14.2, 18.5, 19.8, 24.0 and 27.8° corresponding respectively to the (428), (088), (7911), (4814), (6618) and (9321) crystal planes of MIL-100(Fe). Fe_3O_4 has weak diffraction peaks due to its low content [23]. The diffraction peaks of FM/ZnS hybrid material are highly consistent with that of ZnS. With an increase in FM loading, the characteristic crystal peaks of ZnS, such as (002) and (110), are gradually weakened, indicating that a small amount of FM passivates the main exposed crystal surface ZnS. Due to the low FM loading, no FM diffraction peak is observed in the FM/ZnS composite.

3.2. Ftir

Fig. 2 shows the Fourier transform infrared spectra of ZnS, FM and FM/ZnS. It can be seen that the FTIR spectra of the bare ZnS and FM/ZnS composites are highly similar, with characteristic peaks at 608 and 716

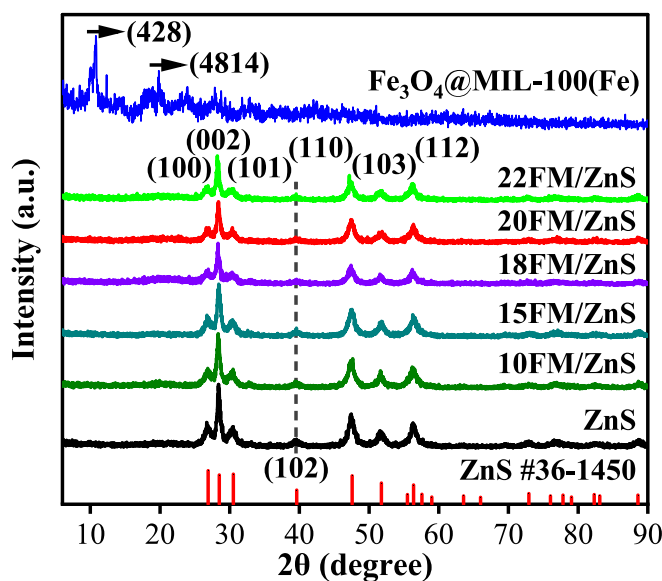


Fig. 1. XRD patterns of ZnS nanoparticles, FM and xFM/ZnS composites.

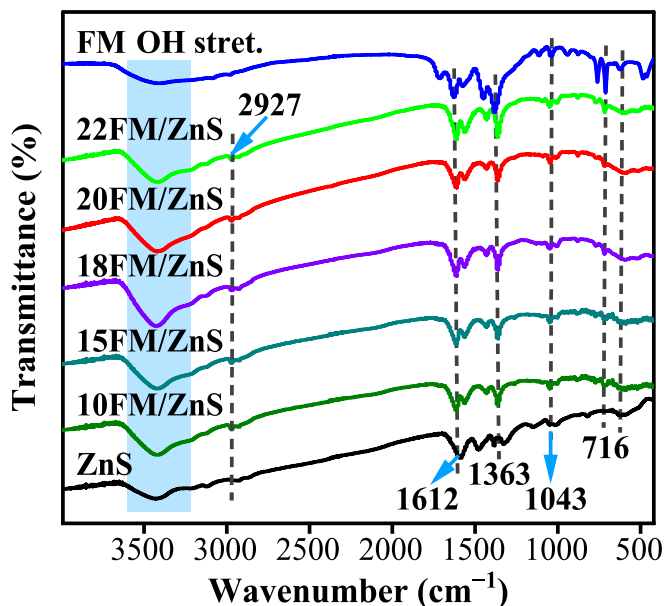


Fig. 2. FT-IR spectrum of ZnS nanoparticles, FM and xFM/ZnS nanocomposites.

cm^{-1} related to the unique stretching vibration bands of sulfur in ZnS [24]. The peak at 1043 cm^{-1} is attributed to the stretching and bending vibration of O_2 , while the peaks at $1363\text{--}1612 \text{ cm}^{-1}$ are attributed to the asymmetric stretching vibration of C–O and C=O. The broad absorption peak at 3430 cm^{-1} is available due to the hydrogen bond's stretching vibration (–OH group), indicating that water molecules are adsorbed on the sample's surface [25]. The characteristic absorption peak of FM is located at 1363 cm^{-1} , indicating a significant asymmetric stretching vibration of C–O. This peak is significant in the composite FM/ZnS as the specific gravity of FM increases. Due to the extremely low content of Fe_3O_4 , it is difficult to locate the Fe–O bond [23]. In summary, FM and ZnS have formed a stable chemical bond structure.

3.3. Tem

TEM, HRTEM and EDS studies were conducted to characterize the

microstructure of 20FM/ZnS nano hybrid material. Fig. 3a is the transmission electron microscope image of 20FM/ZnS, which clearly shows that ZnS presents irregular shuttle-shaped nano-fragmentation with certain aggregation with a particle size between 20 and 60 nm. FM shows a relatively large spherical particle of diameter in the 168–426 nm range. When the loading amount of FM is 20%, the irregular ZnS nanoparticles are partially wrapped in FM, and the unsmooth contact surface provides more reactive sites for the system. Fig. 3b is a high-

resolution TEM image of 20FM/ZnS. The clear and orderly spaced lattice stripes indicate that 20FM/ZnS possesses high crystallinity. The observed lattice fringes at 0.196, 0.294 and 0.330 nm, respectively corresponded to the (110), (101) and (100) crystal faces of wurtzite ZnS nanoparticles [16]. Fig. 3c shows the EDS results of the 20FM/ZnS composite. The sample comprises 33.41, 23.38, 15.81, 13.96 and 13.44 wt% of Zn, S, Fe, C and O, respectively. The elemental distribution diagram in Fig. 3d shows that Zn, S and C show good dispersion while Fe

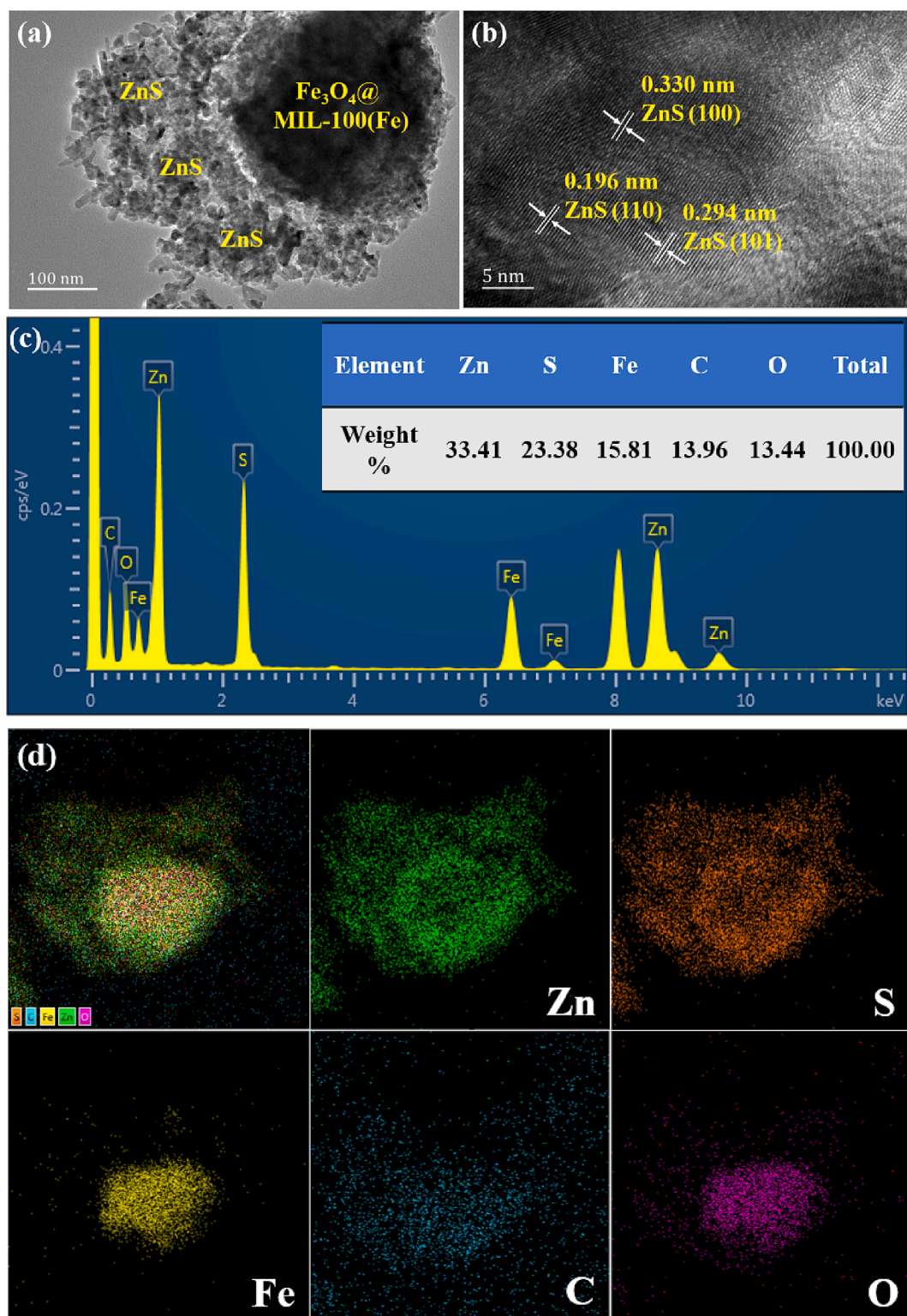


Fig. 3. TEM (a) and HRTEM images of 20FM/ZnS (b), EDS spectrum (c) and element distribution mapping of Zn, S, Fe, C and O in 20FM/ZnS (d).

and O elements agglomerate slightly.

3.4. Xps

Fig. 4a shows the XPS full spectrum of 20FM/ZnS composite, indicating the presence of five elements (Zn, S, Fe, C and O) and is consistent with the EDS results. Fig. 4b shows the XPS peak of Zn 2p. The binding energy peaks at 1021.2 and 1044.3 eV are attributed to the spin-orbital splitting of Zn^{2+} corresponding to Zn 2p_{3/2} and Zn 2p_{1/2}, respectively

[26]. In addition, a signal peak of Zn LM2 appears at 498.5 eV and is caused by the Auger electrons of Zn [27]. Fig. 4c shows the high-resolution spectrum of S 2p with XPS peaks available at 161.4 and 162.5 eV. These peaks correspond to S 2p_{3/2} and S 2p_{1/2} indicating that S exists as S²⁻ in the sample. Fig. 4d shows the XPS spectrum of Fe 2p with three characteristic peaks at 701.5, 715.5 and 724.3 eV. These peaks correspond to Fe 2p_{3/2} and 2p_{1/2} orbitals and indicate that Fe exists as Fe³⁺ [28]. In Fig. 4e, the peaks at the binding energies of 284.6, 285.9 and 288.2 eV come from the carbon and carboxyl functional groups on

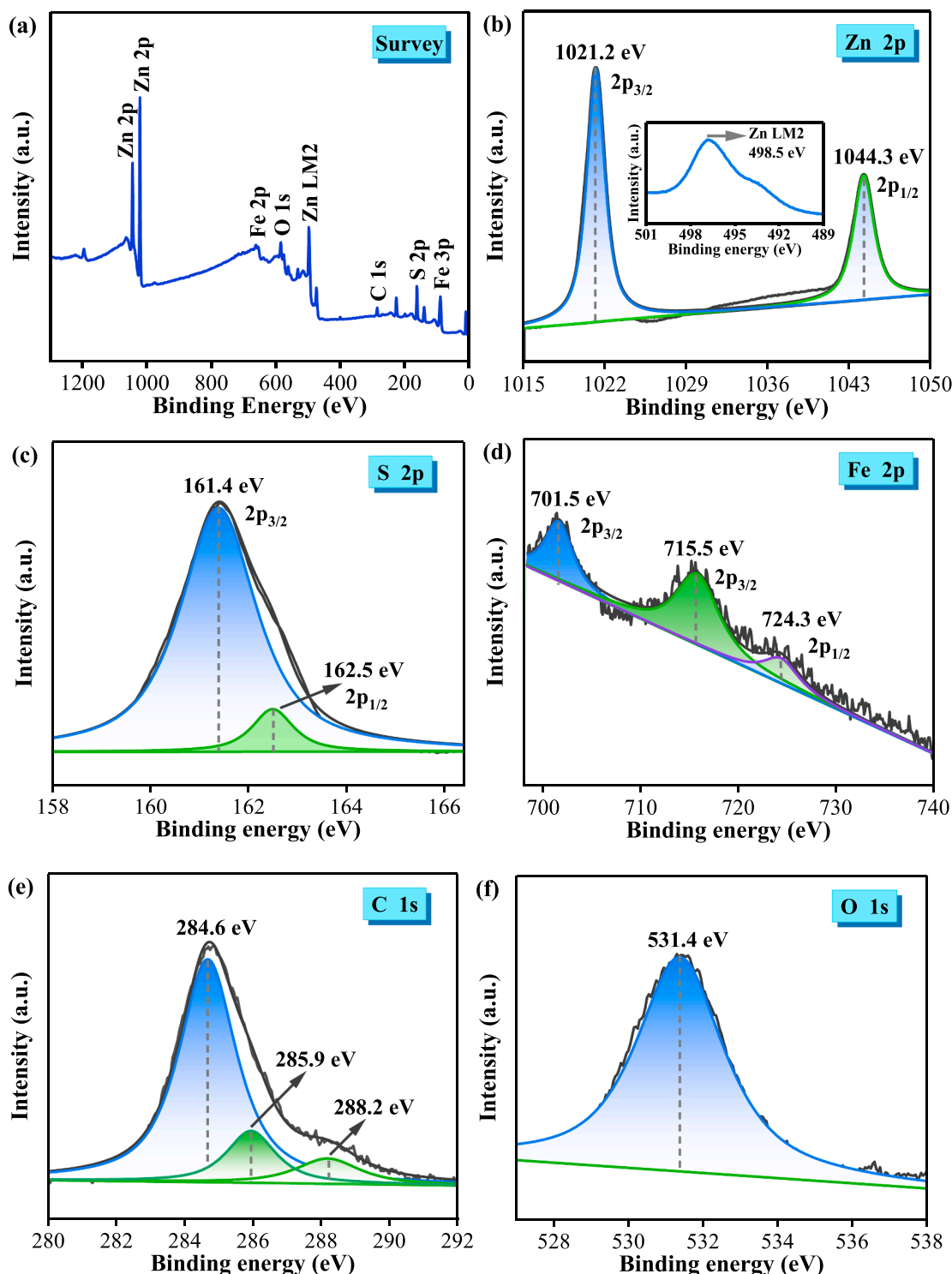


Fig. 4. Full-scan XPS spectrum of 20FM/ZnS composite (a), Zn 2p (b), S 2p (c), Fe 2p (d), C 1s (e), and O 1s (f).

the benzene ring of MIL-100(Fe). Fig. 4f shows the XPS spectrum of O1s with a peak at 531.4 eV attributed to the O and Fe–O bonds in MIL-100(Fe) [23].

3.5. Catalyst activity

The sonocatalytic activities of FM/ZnS nanocomposites were determined by removing tetracycline antibiotics from an aqueous solution. Fig. 5a shows the sonocatalytic degradation curves of tetracycline with ZnS nanoparticles, FM and FM/ZnS. In the presence of 1 mL H₂O₂, all the catalysts have a strong ability to remove tetracycline by ultrasound, and the sonocatalytic removal rate is the strongest during the first 5 min. Among the prepared catalysts, 20FM/ZnS composite has the best performance in the sonodegradation of tetracycline with a removal rate of 64.83% in 20 min which is twice the removal rate of bare ZnS (35.82%) nanoparticles. The ability of ZnS to remove tetracycline by sonocatalytic enhances with an increase in FM loading. The degradation activity is the highest when the FM loading reaches 20%. When the FM load is 22%, the sonocatalytic activity of the composite slightly decreases, indicating that excessive loading masks the active sites of ZnS. Due to the excessive adhesion of ZnS nanoparticles to the FM surface, agglomeration occurs, which hinders the ability of the catalyst to absorb acoustic waves and reduces its contact interface with pollutants, thereby inhibiting the sonocatalytic activity.

3.6. Investigation of the influencing factors

To investigate the effects of the catalyst dosage, tetracycline concentration, H₂O₂ amount and pH on the sonocatalytic removal of tetracycline, the pollutant removal activities were measured using the optimized sample 20FM/ZnS and the results are provided in Fig. 6. From Fig. 6a, it is clear that as the number of catalyst increases, the sonocatalytic removal of tetracycline first increases and then decreases. This indicates that the excessive addition of 20FM/ZnS can cause agglomeration of the catalyst, which may mask each other's active sites [26]. At the same time, the addition of excessive catalyst has a certain barrier to the propagation of sonoluminescence which reduces the catalytic activity of the catalyst itself [29]. The effect of TC concentration on its sonocatalytic removal is shown in Fig. 6b. The ability of the catalyst to remove tetracycline is inversely proportional to the concentration of tetracycline indicating that high percent of the antibiotic is removed when its concentration is low. When the amount of TC is 30 mg per liter, the sonocatalytic degradation rate is 78.25% in the presence of 1 mL H₂O₂. As shown in Fig. 6c, the amount of H₂O₂ directly impacts the catalyst's activity. In the absence of H₂O₂, only 26.15% TC is removed in 20 min. By changing the amount of H₂O₂ between 0.5 and 2 mL, it has been found that the removal efficiency is the highest in the presence of 1 mL H₂O₂. During sonocatalytic degradation of TC, adding an appropriate amount of H₂O₂ provides sufficient hydroxyl radicals ([•]OH) for

the reaction resulting in an accelerated degradation rate. However, excessive H₂O₂ can act as a scavenger for [•]OH, thereby reducing the sonocatalytic degradation activity of the material [30].

We also checked the sonocatalytic degradation of TC at different pH values [31]. The sonocatalytic degradation of TC increases as the pH value is increased. At a lower pH value, the amount of [•]OH is low, and the degradation is reduced. As the pH value increases, the number of [•]OH free radicals increases, and therefore TC is efficiently removed. At the pH value of 6, the degradation of TC is the highest indicating that a slightly acidic pH environment preferentially assists the ultrasonic degradation of the TC antibiotic.

3.7. Energy band structure

Fig. 7a shows the UV–vis DRS spectra of ZnS, FM and FM/ZnS. The optical absorption band edge of pure ZnS nanoparticles is found at 350 nm, while FM entertains its optical absorption performance in the 200–600 nm range. The absorption band edge of the FM/ZnS composite catalyst is found at 360 nm. Interestingly, the FM/ZnS has a broadened spectral absorption in the 360–600 nm range compared to the pure ZnS nanoparticles. As the amount of FM over ZnS increases, the absorption ability of FM/ZnS continues to increase, indicating that the introduction of FM has an excellent effect on the visible light response of ZnS [32].

The Kubelka-Munk curves were obtained by converting the DRS data of pure ZnS, FM and FM/ZnS using the Tacu equation; $(\alpha h\nu)^n = A(h\nu - E_g)$ where α , h , ν , A and E_g respectively indicate the absorption coefficient, Planck's constant, optical frequency, proportionality constant, and band gap of the semiconductor [33]. ZnS and FM are direct band gap semiconductor materials with an n value of 2 [16,18]. In Fig. 7b, the intercept of the tangent portion of the Kubelka Munk curve from the X-axis is approximately equal to the catalyst band gap. Therefore, the E_g of ZnS, 20FM/ZnS, and FM are 3.66, 3.41 and 2.96 eV, respectively. 20FM/ZnS has significantly enhanced light absorption performance and efficient visible light conversion efficiency.

The flat band potentials of ZnS, 20FM/ZnS, and FM were also measured using the impedance potential method. Fig. 7c shows the Mott-Schottky curves. The positive tangent slope indicates that the catalyst is an n-type semiconductor. According to the intercept between the tangent and the X-axis, the flat band potentials of ZnS, 20FM/ZnS, and FM are respectively –0.56 V, –0.51 V and –0.60 V vs. SCE. In n-type semiconductors, the conduction band potential is approximately equal to the flat band potential [34]. The sample's valence band potential (E_{VB}) can be calculated according to the equation $E_{VB} = E_{CB} + E_g$. Here E_{VB} , E_{CB} , and E_g are the valence band potential, conduction band potential, and band gap, respectively. Thus, the E_{VB} of ZnS, 20FM/ZnS and FM are 3.10, 2.90 and 2.36 eV, respectively.

Fig. 7d is a band structure diagram of ZnS, 20FM/ZnS and FM. The E_g value of the composite material is 0.25 eV lower than that of pure ZnS, indicating that the loading of FM effectively enhances the light

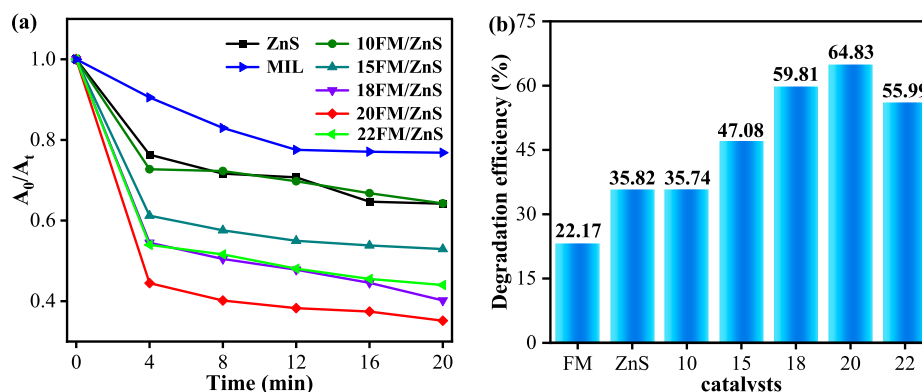


Fig. 5. Ultrasonic degradation curve (a) and removal efficiency of TC over ZnS, FM, and FM/ZnS catalysts (b).

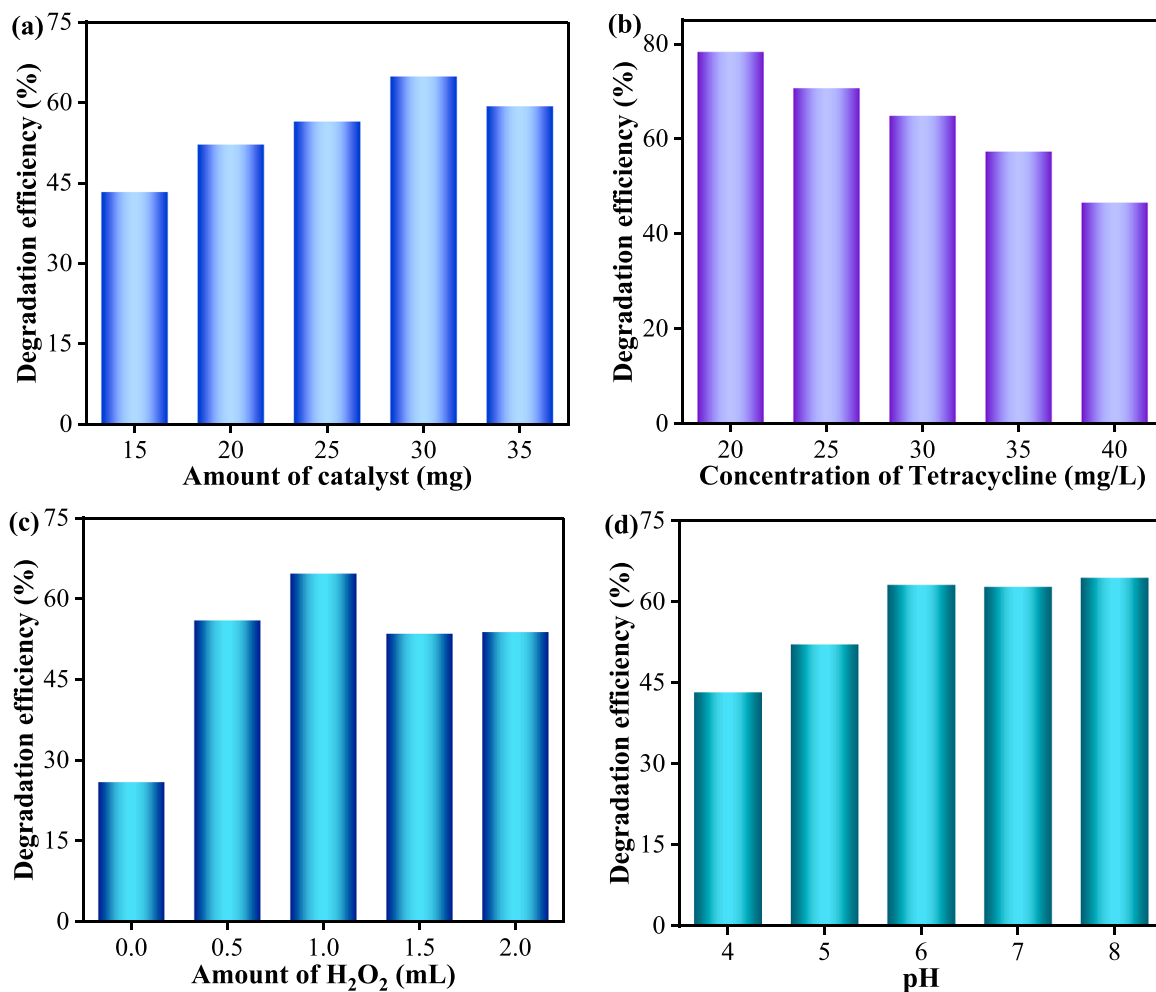


Fig. 6. Effects of the amount of catalyst (a), TC concentration (b), H₂O₂ amount (c) and pH value on the ultrasonic catalytic degradation of TC with 20FM/ZnS (d).

absorption ability of ZnS nanoparticles which is consistent with DRS data.

3.8. Photoelectric performance

Fig. 8a provides the photocurrent responses of pure ZnS nanoparticles, FM and FM/ZnS nanocomposites. After 10 times of light on and off treatment, the catalysts exhibit stable photocurrent responses. Pure ZnS and FM have lower photocurrent densities of 0.2880 and 0.2638 A/cm², respectively. 20FM/ZnS shows significantly enhanced photocurrent with a photocurrent density of 0.9718 μ A/cm², three times larger than pure ZnS and FM. The enhanced photocurrent response indicates that the introduction of FM causes more electrons to be excited, resulting in more photogenerated charges in the system. At the same time, photogenerated electron pairs can be efficiently separated and transported to the catalyst surface in space, thereby quickly participating in the oxidation–reduction reaction over the catalyst surface.

Fig. 8b shows the AC impedance spectra of ZnS, FM and FM/ZnS. The diameter of the semicircular arc represents the charge transfer resistance (Rct). The smaller the semicircular arc, the smaller the catalyst resistance and the higher the charge transfer efficiency [35]. The charge transfer ability of 20FM/ZnS is significantly superior to that of pure ZnS and FM, indicating that the loading of FM provides a more efficient charge transfer path for the ZnS composite system, thereby enabling the catalyst to obtain enhanced sonocatalytic activity.

Photoluminescence (PL) provides effective information about charge separation and recombination in semiconductor materials [36]. As

shown in Fig. 8c, the charge recombination rate in the pure ZnS is very high, and the charge separation situation gradually improves with an increase in the FM ratio. In the composite system, 20FM/ZnS has the best charge separation ability, consistent with photocurrent and impedance spectroscopy results.

The specific surface areas of ZnS and 20FM/ZnS were characterized and analyzed using nitrogen adsorption–desorption tests. As shown in Fig. 8d, 20FM/ZnS has better adsorption–desorption performance. The loading of a small amount of FM provides a larger specific surface area and rich the pore structure of ZnS to provide more active sites for the adsorption of the pollutant particles. During the sonocatalytic degradation process, pollutant particles are more likely to meet the catalyst resulting in enhanced degradation performance.

3.9. Sonocatalytic degradation mechanism of tetracycline

To analyze the Sonocatalytic degradation mechanism of tetracycline, free radical capturing tests were conducted using 20FM/ZnS as a catalyst during the sonocatalytic degradation of TC. The results are shown in Fig. 9. It can be seen that $\cdot\text{O}_2^-$, $\cdot\text{OH}$ and h^+ are the main active degrading species in the sonocatalytic degradation of TC. Of course, H₂O₂ may be the main source of producing a large amount of $\cdot\text{OH}$ during sonocatalysis. The detailed sonocatalytic degradation mechanism needs to be further analyzed through the energy band structure of the semiconductor materials as shown in Fig. 10.

The research based on our experiments has been summarized in the schematic mechanism for the sonocatalytic degradation of TC by FM/

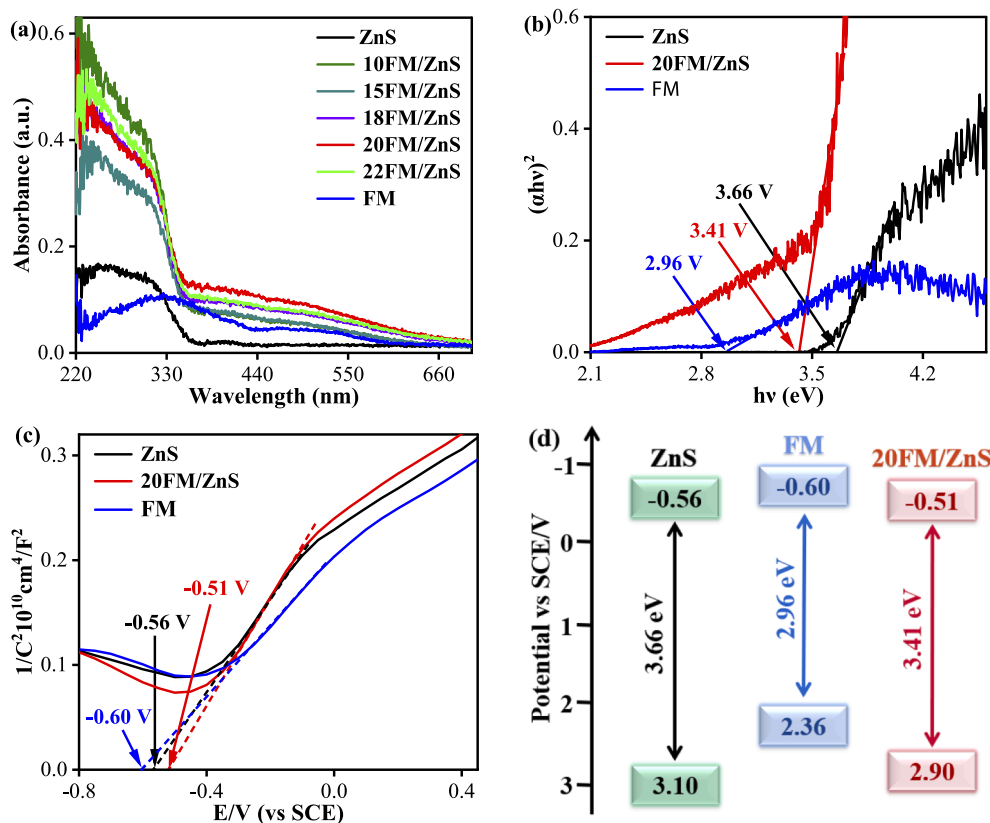
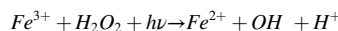
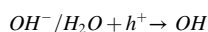
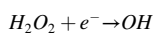
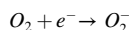


Fig. 7. UV visible diffuse reflectance (a), band gap energy diagram (b), Mott Schottky curves (c) and band structure diagram of ZnS, FM and FM/ZnS catalysts (d).

ZnS nanocomposite, as shown in Fig. 10. The light/heat energy generated during the sonocatalytic process helps to transfer electrons from the valence band to the conduction band of $\text{Fe}_3\text{O}_4@\text{MIL-100}(\text{Fe})$ (FM). At the same time, the sonoluminescence induced by the cavitation effect activates the formation of carriers in the FM/ZnS system [14]. Based on the conduction and valence band potentials of ZnS and FM, there is a certain Fermi energy level difference between the two materials, and electrons easily migrate from the CB of ZnS to VB of FM, forming a stable built-in electric field between the interfaces. Under the strong interaction of Coulomb force, the charge density of ZnS continuously shifts to FM until the Fermi energy levels attain an equilibrium state. Consequently, an S-scheme charge transfer pathway is generated between the ZnS and FM interfaces [37]. The well-established interface results in the transfer and migration of excited charges between the two components providing a service for the excited electrons of ZnS and holes of FM to combine as useless charges. This process significantly allows the excited electrons of FM and holes of ZnS to prolong their lives [38]. Thus, electrons with strong reduction ability in the conduction band of FM and holes with strong oxidation ability in the ZnS valence band are left with prolonged lives to participate in the subsequent acoustic catalytic degradation reaction. During the ultrasonic catalytic degradation, degrading species are generated, which help eradicate the TC antibiotic from the aqueous solution. The generation of these reactive species over FM/ZnS composite catalysts and their reactions with TC are described in the following equations [23]:



The electrons in CB of FM undergo a reduction reaction with H_2O_2 and dissolved O_2 in water to generate highly reactive $\cdot\text{OH}$ and $\cdot\text{O}_2^-$ radicals, which directly attack tetracycline molecules to decompose while holes in the VB of ZnS react with water molecules and OH^- ions to generate more $\cdot\text{OH}$ free radicals to assist the degradation of TC further. Due to the presence of $\text{Fe}_3\text{O}_4@\text{MIL-100}(\text{Fe})$ in the system, the Fenton-like reactions of Fe^{2+} and Fe^{3+} also provide their services to decompose TC. The reaction of Fe^{3+} with H_2O_2 promotes the production of $\cdot\text{OH}$ in the system, which helps to accelerate the sonocatalytic decomposition process of TC. In summary, the enhanced sonocatalytic degradation activity of FM/ZnS nanocomposites for tetracycline is mainly due to the efficient charge separation achieved through the S-scheme heterostructure, the Fenton like reaction of Fe^{2+} and Fe^{3+} cycle, and the strong redox properties of $\cdot\text{OH}$, $\cdot\text{O}_2^-$, and h^+ radicals generated during the degradation process.

4. Conclusion

In summary, this work reports the synthesis of organic-inorganic nanocomposites ($\text{Fe}_3\text{O}_4@\text{MIL-100}(\text{Fe})/\text{ZnS}$) using a simple solvent evaporation method for the efficient sonocatalytic removal of tetracycline from water. Amongst the prepared samples, 20FM/ZnS exhibited the best activity for the removal of TC. After the ultrasonic treatment for 20 min, the removal rate of TC from a solution of 50 mL (20 mg/L) by 30 mg catalyst was 78.25%. The enhanced sonocatalytic activity for the tetracycline removal was attributed to the synergistic effect of multiple factors such as efficient charge separation between FM and ZnS interfaces, increased specific surface area of ZnS providing more active sites, Fenton like reactions of Fe ions, and strong redox potentials of the

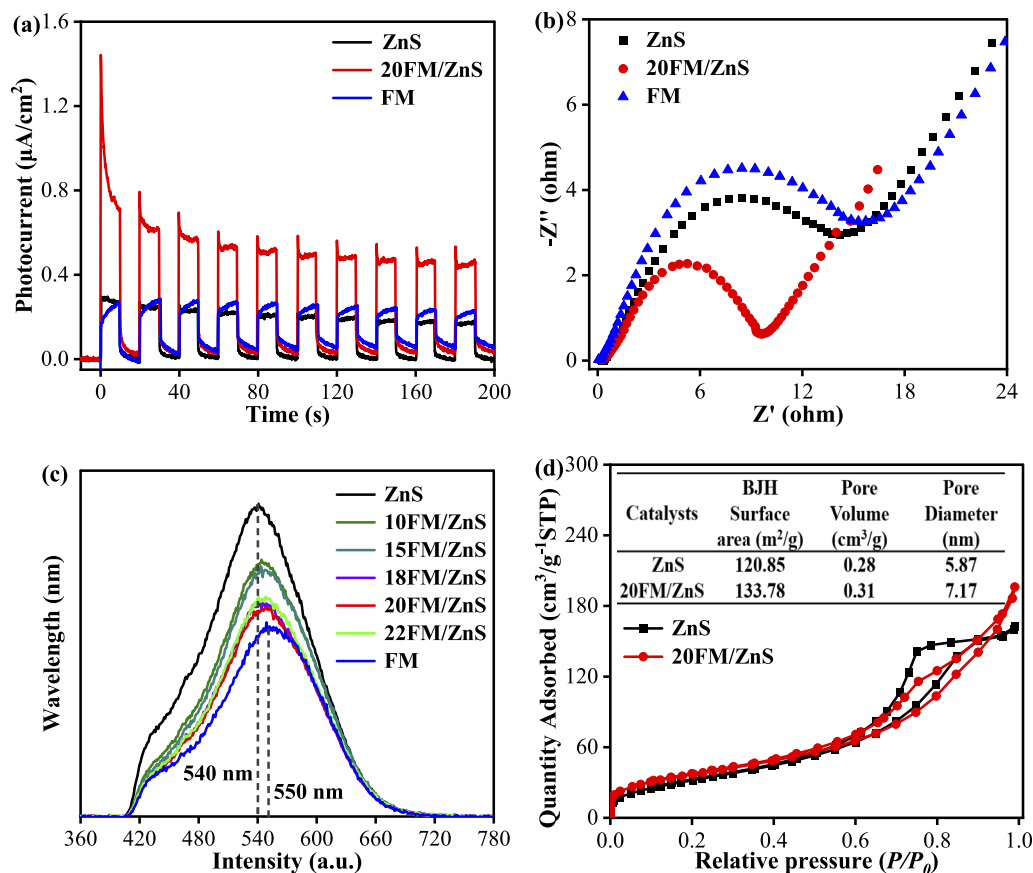


Fig. 8. Photocurrent response (a), and impedance spectra of ZnS, FM and 20FM/ZnS (b), PL spectra of pure ZnS, FM and xFM/ZnS (c) and nitrogen adsorption-desorption isotherms of ZnS and 20FM/ZnS (d).

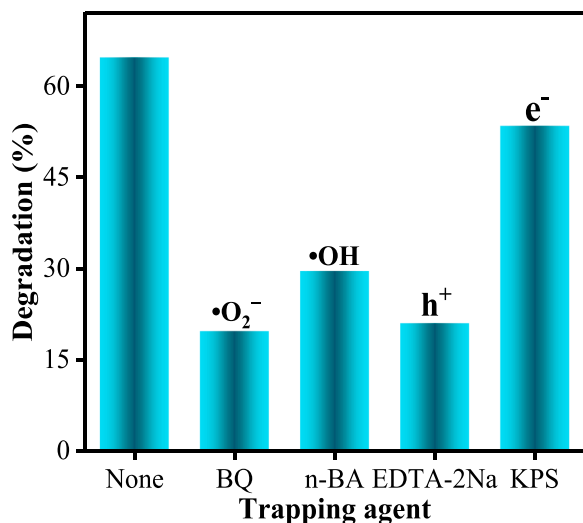


Fig. 9. Active species capturing experiments for the sonocatalytic degradation of TC by 20FM/ZnS.

excited electrons and holes. This study shows that ZnS nanomaterials have broad prospects in the sonocatalytic removal of objectionable pollutants from water.

Declaration of Competing Interest

The authors declare that they have no known competing financial interests or personal relationships that could have appeared to influence

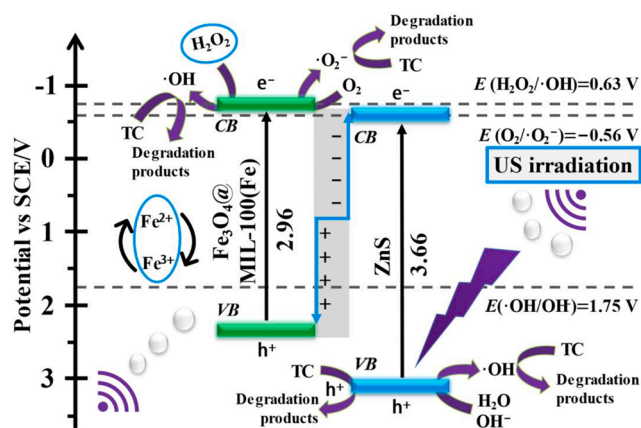


Fig. 10. Schematic diagram for the sonocatalytic degradation of TC over 20FM/ZnS.

the work reported in this paper.

Data availability

No data was used for the research described in the article.

Acknowledgements

This work was financially supported by Science and Technology Project of Hebei Education Department (QN2022182), Transformation and Development Research Fund Project of Baoding University

(2021Z01) and National Natural Science Foundation of China (52272287, 22268003).

References

- [1] S. Zinatloo-Ajabshir, M.S. Morassaei, O. Amiri, M. Salavati-Niasari, L.K. Foong, $\text{Nd}_2\text{Sn}_2\text{O}_7$ nanostructures: Green synthesis and characterization using date palm extract, a potential electrochemical hydrogen storage material, *Ceram. Int.* 46 (2020) 17186–17196.
- [2] A. Saravanan, P.S. Kumar, R.V. Hemavathy, S. Jeevanantham, P. Harikumar, G. Priyanka, D.R.A. Devakirubai, A comprehensive review on sources, analysis and toxicity of environmental pollutants and its removal methods from water environment, *Sci. Total Environ.* 812 (2022), 152456.
- [3] M.S. Morassaei, S. Zinatloo-Ajabshir, M. Salavati-Niasari, $\text{Nd}_2\text{Sn}_2\text{O}_7$ nanostructures: New facile Pechini preparation, characterization, and investigation of their photocatalytic degradation of methyl orange dye, *Adv. Powder Technol.* 28 (2017) 697–705.
- [4] S. Zinatloo-Ajabshir, Z. Salehi, O. Amiri, M. Salavati-Niasari, Green synthesis, characterization and investigation of the electrochemical hydrogen storage properties of $\text{Dy}_2\text{Ce}_2\text{O}_7$ nanostructures with fig extract, *Int. J. Hydrogen Energy* 44 (2019) 20110–20120.
- [5] S. Zinatloo-Ajabshir, Z. Salehi, M. Salavati-Niasari, Green synthesis and characterization of $\text{Dy}_2\text{Ce}_2\text{O}_7$ ceramic nanostructures with good photocatalytic properties under visible light for removal of organic dyes in water, *J. Clean. Prod.* 192 (2018) 678–687.
- [6] R. Hassandoost, A. Kotb, Z. Movafagh, M. Esmat, R. Guegan, S. Endo, W. Jeevasuwan, N. Fukata, Y. Sugahara, A. Khataee, Y. Yamauchi, Y. Ide, E. Doustkhah, Nanoarchitecturing bimetallic manganese cobaltite spinels for sonocatalytic degradation of oxytetracycline, *Chem. Eng. J.* 431 (2022), 133851.
- [7] J. Zhang, A. Bifulco, P. Amato, C. Imparato, K. Qi, Copper indium sulfide quantum dots in photocatalysis, *J. Colloid Interface Sci.* 638 (2023) 193–219.
- [8] S. Zinatloo-Ajabshir, M.S. Morassaei, M. Salavati-Niasari, Eco-friendly synthesis of $\text{Nd}_2\text{Sn}_2\text{O}_7$ -based nanostructure materials using grape juice as green fuel as photocatalyst for the degradation of erythrosine, *Compos. B Eng.* 167 (2019) 643–653.
- [9] S. Anandan, V. Kumar Ponnusamy, M. Ashokkumar, A review on hybrid techniques for the degradation of organic pollutants in aqueous environment, *Ultrason. Sonochem.* 67 (2020), 105130.
- [10] J. Abdi, A.J. Sisi, M. Hadipoor, A. Khataee, State of the art on the ultrasonic-assisted removal of environmental pollutants using metal-organic frameworks, *J. Hazard. Mater.* 424 (2022), 127558.
- [11] S. Zinatloo-Ajabshir, M. Salavati-Niasari, Facile route to synthesize zirconium dioxide (ZrO_2) nanostructures: structural, optical and photocatalytic studies, *J. Mol. Liq.* 216 (2016) 545–551.
- [12] K. Qi, C. Zhuang, M. Zhang, P. Gholami, A. Khataee, Sonochemical synthesis of photocatalysts and their applications, *J. Mater. Sci. Technol.* 123 (2022) 243–256.
- [13] Y.-C. Liu, J.-Q. Wang, Y. Wang, C.-L. Chen, X. Wang, Z. Xiang, Sonocatalytic degradation of ciprofloxacin by $\text{BiOBr}/\text{BiFeO}_3$, *Appl. Catal. A* 643 (2022), 118776.
- [14] L. Xu, X.-Q. Wu, C.-Y. Li, N.-P. Liu, H.-L. An, W.-T. Ju, W. Lu, B. Liu, X.-F. Wang, Y. Wang, X. Wang, Sonocatalytic degradation of tetracycline by $\text{BiOBr}/\text{FeWO}_4$ nanomaterials and enhancement of sonocatalytic effect, *J. Clean. Prod.* 394 (2023), 136275.
- [15] M. Dastborhan, A. Khataee, S. Arefi-Oskoui, Y. Yoon, Synthesis of flower-like MoS_2/CNTs nanocomposite as an efficient catalyst for the sonocatalytic degradation of hydroxychloroquine, *Ultrason. Sonochem.* 87 (2022), 106058.
- [16] J.C. Murillo-Sierra, A. Hernández-Ramírez, Z.-Y. Zhao, A. Martínez-Hernández, M. A. Gracia-Pinilla, Construction of direct Z-scheme WO_3/ZnS heterojunction to enhance the photocatalytic degradation of tetracycline antibiotic, *J. Environ. Chem. Eng.* 9 (2021), 105111.
- [17] A. Mandal, S. Mandi, B. Mukherjee, Ultrasound aided sonocatalytic degradation of Rhodamine B with graphitic carbon nitride wrapped zinc sulphide nanocatalyst, *Ceram. Int.* 48 (2022) 10271–10279.
- [18] W. He, Z. Li, S. Lv, M. Niu, W. Zhou, J. Li, R. Lu, H. Gao, C. Pan, S. Zhang, Facile synthesis of $\text{Fe}_3\text{O}_4/\text{MIL-100}(\text{Fe})$ towards enhancing photo-Fenton like degradation of levofloxacin via a synergistic effect between Fe_3O_4 and MIL-100 (Fe), *Chem. Eng. J.* 409 (2021), 128274.
- [19] T. Sadeghi Rad, A. Khataee, S. Arefi-Oskoui, S. Sadeghi Rad, Y. Orooji, E. Gengec, M. Kobya, Graphene-based ZnCr layered double hydroxide nanocomposites as bactericidal agents with high sonophotocatalytic performances for degradation of rifampicin, *Chemosphere* 286 (2022), 131740.
- [20] D. Zhou, X. Chen, B. Liang, X. Fan, X. Wei, J. Liang, L. Wang, Embedding MIL-100 (Fe) with magnetically recyclable Fe_3O_4 nanoparticles for highly efficient esterification of diterpene resin acids and the associated kinetics, *Microporous Mesoporous Mater.* 289 (2019), 109615.
- [21] R. Kayisier, Y. Ma, K. Qi, L. Xiao, Y. Wang, Y. Li, J. Li, Y. Li, Synergetic removal of mixed pollutants over cerium oxide/red phosphorus heterojunction composite, *Vacuum* 213 (2023), 112068.
- [22] S. Sarwar, M.C. Lin, C. Amezcaga, Z. Wei, E. Iyayi, H. Polk, R. Wang, H. Wang, X. Zhang, Ultrasensitive electrochemical biosensors based on zinc sulfide/graphene hybrid for rapid detection of SARS-CoV-2, *Adv. Compos. Hybrid Mater.* 6 (2023) 49.
- [23] W. He, H. Jia, Z. Li, C.-Q. Miao, R. Lu, S. Zhang, Z. Zhang, Magnetic recyclable $\text{g-C}_3\text{N}_4/\text{Fe}_3\text{O}_4/\text{MIL-100}(\text{Fe})$ ternary catalyst for photo-Fenton degradation of ciprofloxacin, *J. Environ. Chem. Eng.* 10 (2022), 108698.
- [24] A. Fazli, F. Zakeri, A. Khataee, Y. Orooji, A $\text{BaTiO}_3/\text{WS}_2$ composite for piezo-photocatalytic persulfate activation and ofloxacin degradation, *Commun. Chem.* 5 (2022) 95.
- [25] S. Moshtaghi, S. Zinatloo-Ajabshir, M. Salavati-Niasari, Preparation and characterization of BaSnO_3 nanostructures via a new simple surfactant-free route, *J. Mater. Sci. Mater. Electron.* 27 (1) (2016) 425–435.
- [26] J. Zhang, X. Gu, Y. Zhao, K. Zhang, Y. Yan, K. Qi, Photocatalytic hydrogen production and tetracycline degradation using ZnIn_2S_4 quantum dots modified $\text{g-C}_3\text{N}_4$ composites, *Nanomaterials* 13 (2023) 305.
- [27] Z. Xu, Z. Zhang, M. Li, H. Yin, H. Lin, J. Zhou, S. Zhuo, Three-dimensional ZnS/reduced graphene oxide/polypyrrole composite for high-performance supercapacitors and lithium-ion battery electrode material, *J. Solid State Electrochem.* 23 (2019) 3419–3428.
- [28] J. Song, J. Zhang, A. Zada, Y. Ma, K. Qi, $\text{CoFe}_2\text{O}_4/\text{NiFe}_2\text{O}_4$ S-scheme composite for photocatalytic decomposition of antibiotic contaminants, *Ceram. Int.* 49 (2022) 12327–12333.
- [29] M. Rezaeyeenik, M. Mousavi-Kamazani, S. Zinatloo-Ajabshir, CeVO_4/rGO nanocomposite: facile hydrothermal synthesis, characterization, and electrochemical hydrogen storage, *Appl. Phys. A* 129 (2023) 47.
- [30] R. Liang, S. Luo, F. Jing, L. Shen, N. Qin, L. Wu, A simple strategy for fabrication of $\text{Pd}/\text{MIL-100}(\text{Fe})$ nanocomposite as a visible-light-driven photocatalyst for the treatment of pharmaceuticals and personal care products (PPCPs), *Appl. Catal. B* (2015).
- [31] Y. Ma, X. Aihemaiti, K. Qi, S. Wang, Y. Shi, Z. Wang, M. Gao, F. Gai, Y. Qiu, Construction of oxygen-vacancies-rich S-scheme $\text{BaTiO}_3/\text{red phosphorus}$ heterojunction for enhanced photocatalytic activity, *J. Mater. Sci. Technol.* 156 (2023) 217–229.
- [32] S. Zinatloo-Ajabshir, E. Shafaati, A. Bahrami, Facile fabrication of efficient $\text{Pr}_2\text{Ce}_2\text{O}_7$ ceramic nanostructure for enhanced photocatalytic performances under solar light, *Ceram. Int.* 48 (2022) 24695–24705.
- [33] K. Qi, X. Xing, A. Zada, M. Li, Q. Wang, S.-Y. Liu, H. Lin, G. Wang, Transition metal doped ZnO nanoparticles with enhanced photocatalytic and antibacterial performances: experimental and DFT studies, *Ceram. Int.* 46 (2) (2020) 1494–1502.
- [34] Y. Liu, Q. Zhang, B. Yang, J. Xu, Y.a. Yan, J. He, Synthesis of Zn^{2+} doped AgIn_3S_7 sub-microspheres and its visible light photocatalytic activity, *J. Mater. Sci. Mater. Electron.* 30 (16) (2019) 15257–15266.
- [35] M.F. Khan, S.u.H. Bakhtiar, A. Zada, F. Raziq, H.A. Saleemi, M.S. Khan, P. Muhammad Ismail, A.C. Alguno, R.Y. Capangpangan, A. Ali, S. Hayat, S. Ali, A. Ismail, M. Zahid, Ag modified ZnO microspheres synthesis for efficient sonophotocatalytic degradation of organic pollutants and CO_2 conversion, *Environ. Nanotechnol., Monit. Manage.*, 18 (2022) 100711.
- [36] Y. Zhao, A. Zada, Y. Yang, J. Pan, Y. Wang, Z. Yan, Z. Xu, K. Qi, Photocatalytic removal of antibiotics on $\text{g-C}_3\text{N}_4$ using amorphous CuO as cocatalysts, *Front. Chem.* 9 (2021), 797738.
- [37] L. Zhang, J. Zhang, H. Yu, J. Yu, Emerging S-scheme photocatalyst, *Adv. Mater.* 34 (2022) 2107668.
- [38] J. Zhang, L. Wang, M. Mousavi, J.B. Ghasemi, J. Yu, Molecular-level engineering of S-scheme heterojunction: the site-specific role for directional charge transfer, *Chin. J. Struct. Chem.* 41 (2022) 3–5.